DRAFT VERSION OCTOBER 1, 2023
Typeset using LaTeX **twocolumn** style in AASTeX63

Environments of luminous low-frequency radio galaxies since cosmic noon: jet-mode feedback dominates in groups at $z \lesssim 1$

GRAYSON C. PETTER [1], RYAN C. HICKOX [1], LEAH K. MORABITO [2], AND DAVID M. ALEXANDER [2]

[1] *Department of Physics and Astronomy, Dartmouth College, 6127 Wilder Laboratory, Hanover, NH 03755, USA*
[2] *Centre for Extragalactic Astronomy, Department of Physics, Durham University, Durham DH1 3LE, UK*

ABSTRACT

Coupling between relativistic jets launched by accreting supermassive black holes and the surrounding gaseous media is a vital ingredient in galaxy evolution models. To constrain the environments in which this feedback takes place over cosmic time, we study the host halo properties of luminous low-frequency radio galaxies ($L_{150\ \mathrm{MHz}} \gtrsim 10^{25}$ W/Hz) selected with the LOw Frequency ARray out to $z \sim 2.5$ through tomographic clustering and cosmic microwave background lensing measurements. We find that these systems occupy massive halos of $\sim 10^{13} - 10^{13.5} h^{-1} M_{\odot}$, exhibiting little evolution over the past $\sim$11 Gyr. The relatively mild evolution of both the clustering and the luminosity function implies that the duty cycle of these systems remains a constant $\sim 10\%$ at $z < 2.5$; i.e. a significant fraction of group-scale halos ($\gtrsim 10^{13} h^{-1} M_{\odot}$) host a powerful low-frequency radio galaxy across time. We estimate the characteristic kinetic heating energy injected per group-scale halo, finding that radio galaxies of the luminosities probed here dominate over radiative wind heating from quasars since at least $z \lesssim 1$. The hosts of luminous radio galaxies at cosmic noon are likely the progenitors of massive galaxy groups in the local universe with quiescent populations, consistent with jet activity as an instrumental source of disruptive feedback.

1. INTRODUCTION

Galaxies form in the standard Λ-cold dark matter cosmology when baryons cool onto collapsed dark matter halos (White & Rees 1978; White & Frenk 1991). However, galaxy formation models which incorporate only the first-order baryonic physics such as gravitational shock-heating and radiative cooling fail to match a wide array of observations of the most massive systems, galaxy groups and clusters. In particular, the efficiency of gas cooling and in turn galaxy growth is observed to be poorer than these models predict in more massive systems (Balogh et al. 2001; Benson et al. 2003; Borgani et al. 2004; Somerville et al. 2008; Donahue & Voit 2022).

The advent of the ROSAT, *Chandra* and *XMM-Newton* X-ray telescopes revealed an unexpected abundance of hot gas in clusters and groups. The cooling time of X-ray gas cores in clusters, groups, and elliptical galaxies is observed to be much shorter than the ages of the systems (Edge et al. 1992; Cavagnolo et al. 2008; Dunn & Fabian 2008), implying that thermal energy must be resupplied by an internal mechanism (Tabor & Binney 1993; Binney & Tabor 1995).

Corresponding author: Grayson Petter
Grayson.C.Petter.GR@dartmouth.edu

It is now recognized that a supermassive black hole (SMBH) lies at the center of every massive galaxy (Magorrian et al. 1998; Kormendy & Ho 2013), and that accretion onto this object triggers active galactic nucleus (AGN) activity which plays an integral role in shaping the host galaxy's growth and evolution through feedback processes (Best et al. 2006; McNamara & Nulsen 2007; Cattaneo et al. 2009; McNamara & Nulsen 2012; Fabian 2012; Alexander & Hickox 2012; Heckman & Best 2014; Hardcastle & Croston 2020). This picture was cemented theoretically when cosmological semi-analytic and hydrodynamic simulations including AGN feedback were able to address the cooling flow problem and reproduce observed local stellar mass functions (Croton et al. 2006; Bower et al. 2006; McCarthy et al. 2010).

This AGN feedback can take one of two forms, jet/radio-mode where relativistic jets are launched by inefficient accretion, and quasar/wind-mode where radiatively-driven winds are spawned by efficient accretion. The discovery of X-ray cavities coincident with radio jets (Boehringer et al. 1993; Carilli et al. 1994; Fabian et al. 2006) provided evidence for jet-mode feedback in the aforementioned groups and clusters. These systems serve as laboratories with which to estimate the jet energy deposition (McNamara et al. 2000; Churazov et al. 2000; Bîrzan et al. 2004, 2008; Cavagnolo et al. 2010), showing that the mechanical power can greatly exceed

that of the synchrotron luminosity, enough to inflate and heat the atmospheres of groups and clusters.

Alternatively, radiation pressure from efficient accretion can drive quasar/wind-mode feedback (Silk & Rees 1998; Elvis 2000; Veilleux et al. 2005; Di Matteo et al. 2005; Springel et al. 2005; Hopkins et al. 2006; Thacker et al. 2006; Laha et al. 2021), evidenced by observed gaseous outflows coincident with quasar activity (Alexander et al. 2010; Rupke & Veilleux 2011; Harrison et al. 2012, 2014; Greene et al. 2014; Brusa et al. 2015; Zakamska et al. 2016; Fiore et al. 2017). However to date, the complete picture of the relative role that jet-mode and wind-mode feedback play is elusive. Radio galaxies are thought to be preferentially triggered by an advection-dominated accretion flow (Narayan & Yi 1994), when the SMBH is fed by condensing hot gas in a massive halo. Meanwhile, quasar activity is generated by a thin accretion disk (Shakura & Sunyaev 1973), expected to be fed by cold gas streams in lower-mass halos. This suggests that jet-mode and wind-mode feedback may be expected to occur in different environments.

Modern hydrodynamic and semi-analytic galaxy evolution models routinely implement feedback from AGNs and match a wide array of observables (Gonzalez-Perez et al. 2014; Vogelsberger et al. 2014; Schaye et al. 2015; Somerville & Davé 2015; Croton et al. 2016; Kaviraj et al. 2017; Springel et al. 2018; Davé et al. 2019; Rennehan et al. 2023). However, feedback effects typically take place on smaller scales than the resolution elements of simulations, such that models must assume "sub-grid" prescriptions. For a complete understanding of AGN feedback, observations are required to constrain which flavor of feedback dominates, and in which environments. Therefore in this work, we study the environments in which luminous low-frequency radio galaxies occur over the past ~ 11 Gyr.

Radio galaxies at $z < 1$ cluster strongly, found in halos of masses $\sim 10^{13.2} - 10^{13.5} h^{-1} M_\odot$ (Magliocchetti et al. 2004; Mandelbaum et al. 2009; Hickox et al. 2009), implying they typically deposit their energy into group environments. It is important to study the environments radio galaxies occupied around "cosmic noon" ($z \sim 2$), when the cosmic star formation efficiency began to decline presumably due to AGN feedback (Madau & Dickinson 2014). To date, relatively few studies have explored the clustering of radio galaxies at $z > 1$, which have been confined to small fields, and conducted at GHz frequencies (Lindsay et al. 2014; Magliocchetti et al. 2017; Hale et al. 2018). Recent advances in low-frequency radio surveys such as with the LOw-Frequency ARray (LOFAR; van Haarlem et al. 2013) offer a new window on radio galaxy clustering. The depth and area curate an unprecedentedly large radio AGN sample, and the low frequency observations reveal the old electron populations and thus likely better trace the long-term energy input of jets into their surroundings.

In this work, we study the host halo environments of ~ 0.5 million luminous radio galaxies selected at low frequencies using the LOFAR telescope with tomographic clustering and lensing measurements. We find that luminous radio galaxies ($L_{150\ \mathrm{MHz}} \gtrsim 10^{25}$ W/Hz) occupy massive halo environments ($\sim 10^{13} - 10^{13.5} h^{-1} M_\odot$) at $z < 2.5$. We estimate the duty cycle of these radio galaxies to be a near constant $\sim 10\%$, a significant fraction of massive halos host a powerfully-interacting jet at a given time. We also estimate the average kinetic heating energy released by these systems per host halo, finding that jet-mode heating dominates over wind mode in group-scale halos at $z \lesssim 1$.

Throughout this work, we adopt a "Planck 2018" CMB+BAO Λ-CDM concordance cosmology (Planck Collaboration et al. 2020), with $h = H_0/100$ km s^{-1}Mpc^{-1} = 0.6766, $\Omega_m = 0.3111$, $\Omega_\Lambda = 0.6888$, $\sigma_8 = 0.8102$, and $n_s = 0.9665$. We adopt the convention where synchrotron spectra are parameterized as $S_\nu \propto \nu^\alpha$, and perform k-corrections throughout using a spectral index of $\alpha = -0.7$. Any magnitudes are presented in the Vega system.

2. DATA

In this work, we study the clustering properties of radio galaxies selected at 150 MHz using LOFAR data. We also study the redshift evolution of their clustering properties by cross-correlating their positions with spectroscopic galaxy samples from the Sloan Digital Sky Survey (SDSS; York et al. 2000).

2.1. *The LOFAR Two-metre Sky Survey*

The LOFAR is a sensitive interferometric telescope currently revolutionizing surveys of the radio sky. In particular, the pioneering LOFAR Two-metre Sky Survey (LoTSS; Shimwell et al. 2017) is the first to produce deep (RMS ~ 100 μJy beam^{-1}) and high-resolution ($6''$) maps at low frequencies (~ 150 MHz) over a wide area, and represents an order of magnitude sensitivity improvement for typical sources over the Faint Images of the Radio Sky at Twenty-centimeters (FIRST) survey (Becker et al. 1995; Helfand et al. 2015), conducted at 1.4 GHz. The second data release of LoTSS-wide (DR2; Shimwell et al. 2022) covers 5634 deg^2 and catalogs 4,396,228 sources.

This is a premier dataset to study radio galaxy clustering (Siewert et al. 2020; Tiwari et al. 2022) as a probe of feedback for a variety of reasons. The detection depth surpasses the switch point of ~ 1.5 mJy below which star-forming galaxies and radio-quiet AGNs become the dominant populations (Best et al. 2023), and therefore a deeper survey would not select a larger sample of radio galaxies on the basis of flux alone. The wide area is useful for statistical power in

clustering measurements due to the inherent rarity of luminous radio galaxies, and the survey footprint significantly overlaps with that of the SDSS, enabling cross-correlations with spectroscopic samples. The high angular resolution allows accurate identification of optical/infrared counterparts (e.g., Hardcastle et al. 2019; Gürkan et al. 2019) for source classification and redshift estimation. Finally, low-frequency observations are well-suited to tracing the environments in which feedback may be taking place, as they are more sensitive to steep-spectrum, lobe-dominated sources which better trace the long-term integrated power input into their surroundings than GHz frequencies, which are more sensitive to core-dominated or beamed emission.

We adopt the source catalog presented in Hardcastle et al. (2023), which has attempted to associate double-lobed duplicate detections into single sources, and match to optical (Dey et al. 2019) or infrared (Schlafly et al. 2019) counterparts when possible, though using this rather than the raw DR2 catalog appears to make no difference in our results.

2.2. *eBOSS Quasar Sample*

One of the goals of this work is to study radio galaxy clustering and its evolution at $z > 1$. We therefore utilize quasars with spectroscopic redshifts from SDSS surveys as matter tracers for cross-correlations with LoTSS-selected radio galaxies at $1 < z < 3$.

The Extended Baryon Oscillation Spectroscopic Survey (eBOSS; Dawson et al. 2016) was a spectroscopic survey designed to measure baryon acoustic oscillations in the distribution of three tracers, star-forming emission-line galaxies, luminous red galaxies, and quasars. The quasar sample tracing high-redshift structure consists of 343,708 uniformly targeted (Myers et al. 2015) systems at $0.8 < z < 2.2$, and 72,667 at $2.2 < z < 3.5$, representing the largest statistical sample of spectroscopic quasars to date. The eBOSS collaboration has produced large-scale structure catalogs including randoms and weights for measuring unbiased correlation functions (Ross et al. 2020). We utilize the versions presented in Rezaie et al. (2021), including quasars at $z > 2.2$ and incorporating updated systematic weights. We combine the data from the north and south galactic caps, as we find that the small differences in redshift distribution and bias between the hemispheres are negligible for the purpose of this work.

2.3. *BOSS Galaxy Sample*

When investigating the clustering of luminous radio galaxies at low redshift ($0.25 < z < 0.5$), we find that the sample is too sparse for useful autocorrelation measurements. We therefore cross-correlate low redshift radio galaxies with more numerous SDSS BOSS (Dawson et al. 2013) galaxies at $0.25 < z < 0.5$ for increased precision.

The BOSS targeted red-sequence galaxies at $z < 0.7$ of roughly constant stellar mass (CMASS) as highly-biased tracers of the large-scale structure. We utilize the combined catalog (Reid et al. 2016) of CMASS ($0.4 < z < 0.7$) and LOWZ ($z < 0.4$) galaxies to cross-correlate with radio galaxies at relatively low redshift.

2.4. *LoTSS-deep Data*

To aid in interpreting our clustering measurements, we make use of derived data products from the LoTSS-deep survey DR1 (Tasse et al. 2021; Sabater et al. 2021). This lies amongst the deepest (RMS ~ 20 μJy) radio surveys to date, covering more than an order of magnitude wider area than the comparable depth VLA-COSMOS survey (Smolčić et al. 2017), totaling 25 deg^2 with overlapping deep multi-wavelength photometry in the Boötes, Lockman-hole, and ELAIS-N1 fields. This photometry allows for host identification (Kondapally et al. 2021), photometric redshift estimation (Duncan et al. 2021), source classification, and host galaxy property constraint through spectral energy decomposition (Best et al. 2023), and the estimation of the radio AGN and star formation luminosity functions (Kondapally et al. 2022). The redshift information is crucial to our clustering and lensing analysis, and the luminosity functions will allow estimation of the occupation statistics when combined with clustering measurements. The depth of the survey is sufficient to uncover most of the radio AGN luminosity in the universe within the probed volume, such that 90% of the sources near the 150 MHz flux limit are dominated by emission from star formation.

2.5. *Planck Cosmic Microwave Background Lensing Map*

Cosmic microwave background photons emitted during the recombination epoch have been gravitationally-lensed by the intervening structure, and provide a complimentary probe of high-redshift galaxies' host halo properties along with their clustering. A number of high-resolution CMB experiments have now produced wide-area maps of the lensing convergence κ, a projected surface mass density tracing structure from $0.5 \lesssim z \lesssim 5$ (e.g., Planck Collaboration et al. 2020; Omori et al. 2023; Madhavacheril et al. 2023). Only *Planck*'s all-sky survey overlaps with LoTSS DR2, and thus we use the *Planck* final release (PR4) lensing map (Carron et al. 2022) to study the host-halo properties of radio galaxies selected in LoTSS. We also make use of the provided simulated maps to estimate uncertainties. We produce maps from the combined temperature and polarization data (minimum-variance reconstruction) at NSIDE=1024 resolution using ℓ-modes < 2048 for cross-correlation with radio galaxy overdensity maps.

2.6. *WISE Infrared Photometry*

Near-infrared photometric magnitudes and colors can serve as approximate redshift indicators for massive galaxies

(e.g., Schlafly et al. 2019), and we thus use infrared counterparts to radio galaxies to study their clustering evolution. The Wide-field Survey Explorer (*WISE;* Wright et al. 2010) is a space telescope which has mapped the entire sky in four infrared bands, centered at 3.4, 4.6, 12 and 22 μm (named W1, W2, W3, and W4 respectively). *WISE* continues to operate in the two shorter-wavelength bands in its post-cryogenic phase, and the deeper resulting imaging continues to detect fainter and higher-redshift galaxies. We utilize W1 and W2 photometry from the CatWISE2020 (Marocco et al. 2020; Marocco et al. 2021a) catalog matched to LoTSS sources in order to separate them into broad redshift regimes and study the evolution of radio galaxy clustering.

3. RADIO GALAXY SAMPLES

3.1. *High-z Radio Galaxies (HzRGs)*

We aim to study the environments of luminous radio galaxies across cosmic time, including at the relatively unexplored epoch of $z > 1$. However, the subset of LoTSS sources dominated by radio galaxies ($S_{150\ \mathrm{MHz}} \gtrsim 2$ mJy) exhibits a broad redshift distribution peaking at $z \sim 0.5$ with a long tail towards higher redshifts (Duncan et al. 2021; Alonso et al. 2021; Best et al. 2023). In order to study the clustering within a certain redshift range, we can utilize a *tomographic* technique whereby we cross-correlate radio sources with tracer populations of galaxies at known redshift.

While it is possible to perform tomography with the full LoTSS-bright sample, the $\sim 50\%$ of sources at $z < 1$ would add noise to the desired cross-correlations at $z > 1$, and potentially contribute spurious signal due to magnification bias. We therefore attempt to isolate the $z > 1$ population within the LoTSS sample using mid-infrared *WISE* photometry. Aged stellar populations exhibit a negative K-correction out to $z \sim 2$ at observed-frame 3-5 μm, allowing WISE to detect massive galaxies out to $z \sim 2-3$. We leverage the feature that higher-redshift galaxies will appear both redder and fainter in W1/W2 space (Schlafly et al. 2019; Krolewski et al. 2020) to select $z > 1$ radio galaxies.

We match the host galaxy catalog of the bright and AGN-dominated subset ($S_{150\ \mathrm{MHz}} > 2$ mJy) of LoTSS sources (Best et al. 2023) in the Boötes field (which has the best spectroscopic coverage of the LoTSS-deep fields) to the CatWISE catalog with a match radius of 3″ (∼half of the *WISE* PSF), and display the resulting *WISE* diagram in the top panel of Figure 1. Sources are colored by their broad redshift regime and galaxies belonging to redshift epochs cluster together in the diagram, demonstrating that *WISE* magnitudes and colors can be used to isolate radio galaxies at high redshift.

To curate the $z > 1$ sample, we adopt the sliding color cut form of Schlafly et al. (2019) designed to select high redshift galaxies along with a 90% W2 completeness cut (Marocco et al. 2021b), shown in Figure 1 with a red dashed line:

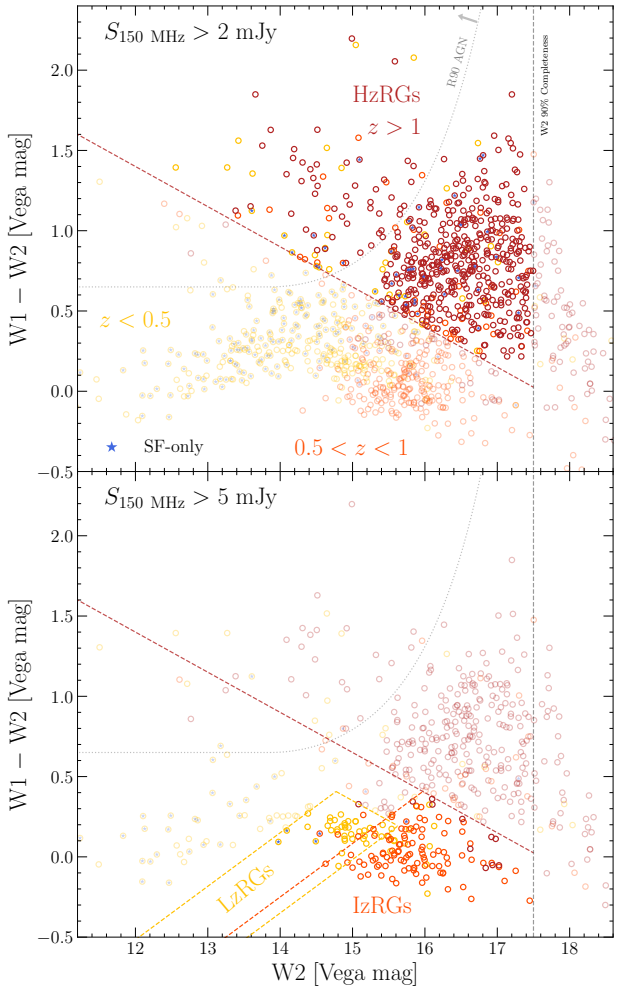

Figure 1. Top panel: A mid-infrared WISE diagram of LoTSS-bright ($S_{150\ \mathrm{MHz}} > 2$ mJy) galaxies in the Boötes field, colored by their broad redshift regime (Duncan et al. 2021; Best et al. 2023), with yellow, orange, and red corresponding to the redshift ranges $z \in [0, 0.5], [0.5, 1], [1, 4]$, respectively. Galaxies in different redshift epochs broadly cluster together in the diagram. We display our sliding color cut for selecting high-redshift $z > 1$ radio galaxies (Eq. 1) with a red dashed line, highlighting the sources satisfying this cut in bold. Bottom panel: the same for $S_{150\ \mathrm{MHz}} > 5$ mJy. An orange line (Eq. 2) selects intermediate-z radio galaxies ($0.5 < z < 1$), and a yellow box (Eq. 3) selects low-z systems ($0.25 < z < 0.5$). The Assef et al. (2018) R90 criterion for selecting radiative-mode quasars is drawn with a gray dotted line; most of these radio galaxies would not be selected as WISE quasars. Sources with radio emission consistent with their far-infrared star formation rates (Best et al. 2023) are highlighted with an additional internal blue star marker, and are mostly confined to low redshifts. Our selections produce radio galaxy samples at $z \sim 0.4$, 0.7, and 1.5, enabling an evolutionary study of their host environments.

$$\begin{cases} S_{150\ \mathrm{MHz}} > 2\ \mathrm{mJy} \\ \mathrm{W1-W2} > (17-\mathrm{W2})/4+0.15, \\ \mathrm{W2} < 17.5 \end{cases} \quad (1)$$

We refer to this sample of bright LoTSS sources with faint/red *WISE* counterparts as our "high-redshift radio galaxy" (HzRG; $z > 1$) sample throughout the rest of the text.

3.2. *Intermediate-z Radio Galaxies (IzRGs)*

We also observe that radio galaxies at $0.5 < z < 1$ cluster together in the *WISE* diagram, and thus extend our study to $z < 1$. For broad correspondence with the luminosities probed by the HzRG sample ($L_{150\ \mathrm{MHz}} \gtrsim 10^{25}$ W/Hz) at lower redshift, we impose a brighter flux threshold of 5 mJy. The *WISE* diagram for such sources is shown in the bottom panel of Figure 1. We show an orange line which when combined with the converse of Eq. 1 forms a selection for intermediate-z radio galaxies (IzRGs, $0.5 < z < 1$):

$$\begin{cases} S_{150\ \mathrm{MHz}} > 5\ \mathrm{mJy} \\ \mathrm{W1-W2} < (17-\mathrm{W2})/4+0.15, \\ \mathrm{W1-W2} < (\mathrm{W2}-17)/3+0.75, \\ \mathrm{W2} < 17.5 \end{cases} \quad (2)$$

3.3. *Low-z Radio Galaxies (LzRGs)*

Finally, we extend our study once more to lower redshift with a color cut designed to select radio galaxies at $0.25 < z < 0.5$. We again further restrict the flux threshold to 20 mJy to probe comparable luminosities with the higher-z samples. We subsequently refer to this sample as low-redshift radio galaxies (LzRGs), shown as a yellow box in Figure 1:

$$\begin{cases} S_{150\ \mathrm{MHz}} > 20\ \mathrm{mJy} \\ \mathrm{W1-W2} < (17-\mathrm{W2})/4-0.15, \\ \mathrm{W1-W2} > (\mathrm{W2}-17)/3+0.65, \\ \mathrm{W1-W2} < (\mathrm{W2}-17)/3+1.15 \end{cases} \quad (3)$$

We note that the bottom panel of Figure 1 shows both the LzRG and IzRG selection with a common flux cut of 5 mJy for visual purposes despite the LzRG selection requiring a stricter 20 mJy cut.

3.4. *Redshift Distributions*

Crucial to interpretation of a clustering or lensing measurement is knowledge of a sample's redshift distribution. After curating the HzRG, IzRG, and LzRG samples using *WISE* data, we estimate their redshift distributions using the LoTSS source-associated redshift catalogs of (Duncan et al. 2021; Best et al. 2023), updated with the new Dark Energy Spectroscopic Instrument (DESI) early release data (DESI Collaboration et al. 2023) for additional spectroscopic redshifts. We estimate the redshift distribution by summing the

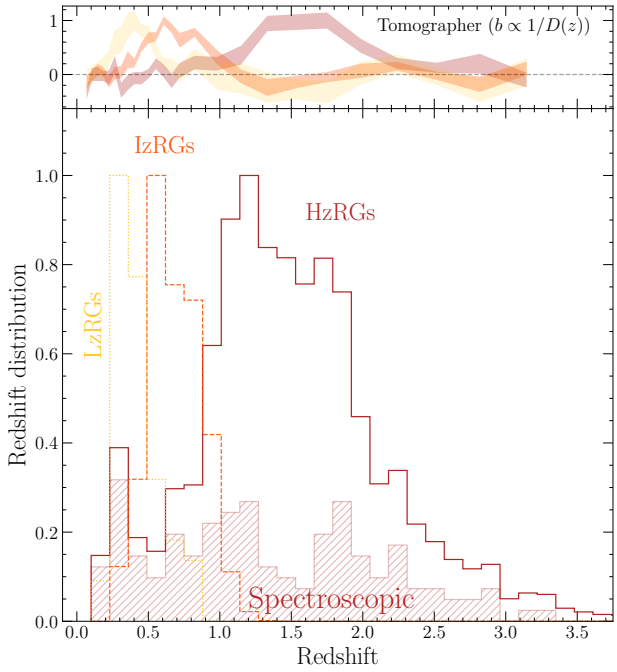

Figure 2. The redshift distributions of the LzRG (yellow), IzRG (orange), and HzRG (red) samples, normalized to maxima of unity for visual clarity. The subset of HzRGs with spectroscopic redshifts are highlighted with a red hatched histogram, and stem mostly from AGES, SDSS, and the DESI EDR, while the total distribution including photo-z PDFs is shown with a solid line. The LzRG and IzRG distributions are predominantly spectroscopic, thus we show their total distributions with yellow dotted and orange dashed lines respectively. The top panel displays corresponding redshift distributions implied from a clustering-based method using the `Tomographer` assuming a fiducial bias dependence (see text). This qualitatively verifies the efficacy of the selection techniques and the validity of the cross-match redshift distributions.

the photo-z probability density functions (PDFs), incorporating spectrosopic redshifts where available. We limit our measurement to the Boötes field for HzRGs and IzRGs, which has the best spectroscopic coverage primarily courtesy of the AGN and Galaxy Evolution Survey (AGES; Kochanek et al. 2012). Due to the relative paucity of LzRGs, we take redshifts from all three LoTSS-deep fields for this sample. We display the resulting redshift distributions in Figure 2. The proposed selections clearly curate samples in distinct redshift regimes, allowing the study of radio galaxy clustering evolution.

To confirm the validity of these cross-match redshift distributions, we derive independent estimates using the clustering redshift technique (Newman 2008; Ménard et al. 2013; Chiang & Ménard 2019), as implemented in the `Tomographer` web tool.[1] This yields a bias-scaled redshift distribution

[1] http://tomographer.org

$b(z)dN/dz$, but untangling any bias evolution from the redshift distribution is degenerate with the goal of this work. Instead, we use this information as a qualitative check on our redshift distributions and assume that the bias evolves inversely with the cosmological growth factor ($b \propto 1/D(z)$; e.g., Alonso et al. 2021). We show the results of the clustering redshift technique in the top panel of Figure 2, confirming that our selections generate radio galaxy samples at three largely distinct redshift epochs. We do not use this clustering-based redshift distribution in any analysis, rather this serves as a qualitative check that our *WISE*-based redshift cuts are performing as intended.

3.5. *Sample Properties*

As LoTSS-deep is complete to radio galaxies significantly fainter than probed here (§2.4), we can use this sample to evaluate the completeness of our selections. Of all the $z > 1$ radio-detected galaxies in the Boötes LoTSS-deep field, 28% of the objects classified as LERGs or HERGs are brighter than 2 mJy. Meanwhile, of the radio galaxies at $0.5 < z < 1$, 17% are brighter than 5 mJy. Finally, x% of $0.25 < z < 0.5$ radio galaxies are brighter than 20 mJy. We conclude that our radio-IR selection recovers approximately the most luminous quarter of radio galaxies at $z \sim 1.5$, and the most luminous fifth at $z \sim 0.7$, and most luminous tenth at $z \sim 0.4$. We note that recovering the remainder of fainter radio galaxies over wide swaths of sky will be challenging without corresponding far-infrared data to disentangle star formation processes. Although we are limited in this study to the luminous end (near the "knee" of the luminosity function; Kondapally et al. 2022), the total kinetic power output of all radio galaxies is dominated by relatively-luminous sources (Kondapally et al. 2023), such that systems of the luminosities considered here contribute roughly half of all the kinetic luminosity density of all radio AGNs. If radio jets are indeed important in shaping galaxy evolution, this sample should thus be significantly representative of the galaxies in which feedback is taking place.

We thus have constructed samples of luminous ($L_{150\ \mathrm{MHz}} \gtrsim 10^{25}$ W/Hz) radio galaxies at low ($z = 0.4$), intermediate ($z = 0.7$), and high redshift ($z = 1.5$) using 150 MHz flux and infrared color criteria in order to probe the host halo environments of low-frequency radio galaxies over cosmic time. We note that this sample is comprised of the most luminous $\sim 10-30$% of radio galaxies. The sample has a low contamination rate by pure SFGs and radio quiet AGN, and is dominated by low-excitation radio galaxies (LERGs), especially at $z < 1$. As noted in Kondapally et al. (2022), this sample is also hosted by predominantly star-forming galaxies at high redshift, transitioning to being hosted almost entirely by luminous passive galaxies at $z < 1$.

3.6. *Masking*

Clustering measurements are sensitive to systematics in the selection function of the given sample of galaxies. It is therefore paramount to characterize the angular selection function of the survey. We characterize the footprint of the LoTSS-wide DR2 using a multi-order coverage (MOC) map.[2] We then stitch together an estimate of the RMS imaging noise from the provided RMS map of each facet,[3] by projecting to a `NSIDE=4096` HEALPix map. Next, we downgrade the map to `NSIDE=128` using the median of the child pixels. Finally, we mask regions of the sky with local median RMS > 0.2 mJy beam^{-1}, totalling only x% of the LoTSS footprint. Our samples of radio sources ($S_{150\ \mathrm{MHz}} > 2$ mJy) are thus expected to be highly complete. However, matching to WISE photometry for redshift information introduces another possible systematic, even though WISE data exists over the entire sky. We observe a decrement in the density of sources at Galactic latitudes near the Galactic plane, possibly due to crowding from increased stellar density. We therefore mask $|b| < 20°$, completing the LoTSS mask we use for radio galaxy autocorrelations. In the case of cross-correlations with eBOSS quasars, we mask the HzRG sample with the eBOSS masks,[4] and correspondingly we mask the eBOSS quasar sample with the LoTSS mask described above.

4. MEASUREMENTS

We perform a variety of measurements to study the halo environments of luminous low-frequency radio galaxies over cosmic time. All correlation function measurements are performed with the `Corrfunc` (Sinha & Garrison 2020) package. We measure correlation functions on comoving projected scales of $5-25\ h^{-1}$Mpc for estimating the linear bias by converting to angular separations given the effective redshift of each sample, unless otherwise stated.

4.1. *Radio Galaxy Autocorrelations*

First, we measure the angular autocorrelation functions of the two luminous radio galaxy samples with sufficient density, IzRGs ($0.5 < z < 1$) and HzRGs ($1 < z < 3$). The angular autocorrelation function is the excess probability above that of a Poisson distribution for detecting a pair of galaxies separated by an angle θ (Peebles 1980). We generate random points within the survey mask (§3.6), and then measure the angular clustering using the (Landy & Szalay 1993) estimator:

$$w(\theta) = \frac{DD - 2DR + RR}{DD}, \tag{4}$$

[2] https://hips.astron.nl/ASTRON/P/lotss_dr2_high/Moc.fits

[3] https://lofar-surveys.org/dr2_release.html

[4] https://data.sdss.org/sas/dr16/eboss/lss/catalogs/DR16/

where *DD*, *DR*, and *RR* are normalized counts for data-data, data-random, and random-random pairs, respectively. We interpret the autocorrelations both with linear and full halo occupation distribution models in (§5). Therefore, we measure the autocorrelations at projected angular scales corresponding to $0.5-25\ h^{-1}$ Mpc for full HOD constraint, but fit only over $5-25\ h^{-1}$Mpc for linear models.

4.2. *Radio Galaxy Tomography*

To probe the redshift evolution of radio galaxy clustering at $z>1$, we also cross-correlate the radio galaxies with samples of galaxies at known redshift, using a tomographic technique. We thus cross correlate HzRGs with eBOSS quasars in redshift slices. After cleaning each sample with the mask of the other, we bin the eBOSS sample into three slices, $1<z<1.5$, $1.5<z<2$, and $2<z<3$. We then measure angular cross-correlations of each slice with the HzRGs, using the Davis & Peebles (1983) estimator:

$$w(\theta) = \frac{D_1 D_2}{D_1 R_2} - 1, \tag{5}$$

where HzRGs and quasars make up the first and second samples, respectively. This estimator depends only on the quasar selection function, which is better quantified than the radio galaxy function. We use the provided quasar weights as specified by Rezaie et al. (2021), while the radio galaxies are weighted to unity. We show the results of these cross-correlations in Figure 3. The measurements are well-fit by linearly biased models, and their bias factors are larger than the bias of quasars being correlated against, implying they occupy more massive halos. We use the same technique when cross-correlating LzRGs with BOSS CMASS galaxies.

4.3. *Matter Tracer Autocorrelations*

In order to interpret the above cross-correlations, we must estimate the bias of the tracer populations being correlated against. Therefore, we measure the projected spatial clustering of the eBOSS quasars and BOSS galaxies in each redshift slice. We first measure the two-dimensional correlation function $\xi(r_p,\pi)$ using the (Landy & Szalay 1993) estimator, before integrating over the line-of sight to the projected correlation function for mitigation of redshift space distortions (Davis & Peebles 1983; Kaiser 1987), up to a maximum line-of-sight separation $\pi_{\rm max} = 40\ {\rm h^{-1}Mpc}$:

$$w_p(r_p) = 2\int_0^{\pi_{\rm max}} d\pi\ \xi(r_p,\pi). \tag{6}$$

4.4. *Radio Galaxy CMB Lensing*

Complimenting the autocorrelation measurement, we acquire an independent constraint on the halos hosting HzRGs using a cross correlation of their positions with the *Planck* CMB lensing convergence (κ) map (§2.5). First, we produce a fractional overdensity (δ) map of radio galaxies at the same NSIDE=1024 resolution as the lensing map:

$$\delta_{RG} = \frac{\rho - \langle\rho\rangle}{\langle\rho\rangle} \tag{7}$$

where ρ represents the galaxy counts-in-cells. We then must estimate the cross-power spectrum of this overdensity map with the Planck map. Harmonic analysis of maps which do not cover the entire sphere induces mode-coupling, such as for surveys with a limited footprint. However, a fast and nearly-optimal estimator to measure an unbiased psuedo-spectrum is implemented in the `NaMASTER` package (Hivon et al. 2002; Alonso et al. 2019). We mask the RG density map (§3.6), and mask the lensing map with the provided mask after apodizing the edges with a 1° FWHM Gaussian. With `NaMASTER`, we measure the cross-spectrum in 10 logarithmically-spaced bins from $200<\ell<2000$. For error estimation, we repeat the above process with 100 provided realizations of simulated lensing maps.

We perform a lensing analysis only of HzRGs for a number of reasons. First, CMB lensing is most efficient at $z\sim 1-2$. Interpretation of the HzRG measurements also relies on photometric redshifts, allowing a comparison of the HzRG lensing and clustering measurements to verify the uncertain redshift distribution (e.g., Petter et al. 2023). The LzRG sample is too sparse and at too low redshift to detect a significant signal. Finally, we observe that a cross-correlation between IzRG positions and CMB lensing is not well-fit by a linear model. This implies contamination in the CMB lensing map from the sources.

5. MODELING

To interpret the clustering measurements and constrain the environments in which radio galaxies release their energy, we model the measurements within a halo model framework (Seljak 2000; Cooray & Sheth 2002). Throughout this section, $\chi(z)$ is the comoving distance, k is the comoving wavenumber, and c is the speed of light. We assume that dark matter halos follow the "NFW" (Navarro et al. 1997) density profile, and the mass-concentration relation of Duffy et al. (2008), where the mass is defined within a radius containing 200 times the universal critical density. We adopt the halo mass function $dn/dM(M,z)$ of Tinker et al. (2008), and the halo mass-bias relation $b(M,z)$ of Tinker et al. (2010). Finally, we utilize `CAMB` (Lewis et al. 2000) to compute all linear matter power spectra $P_{\rm mm}(k,z)$.

An angular correlation function between two matter tracers can be modeled using the Limber (1953) approximation (Peebles 1980; Peacock 1991):

$$w(\theta) = \int dz \frac{dz}{d\chi}\left(\frac{dN}{dz}_i \frac{dN}{dz}_j\right)\int \frac{dk\,k}{2\pi} P_{ij}\, J_0(k\theta\chi), \tag{8}$$

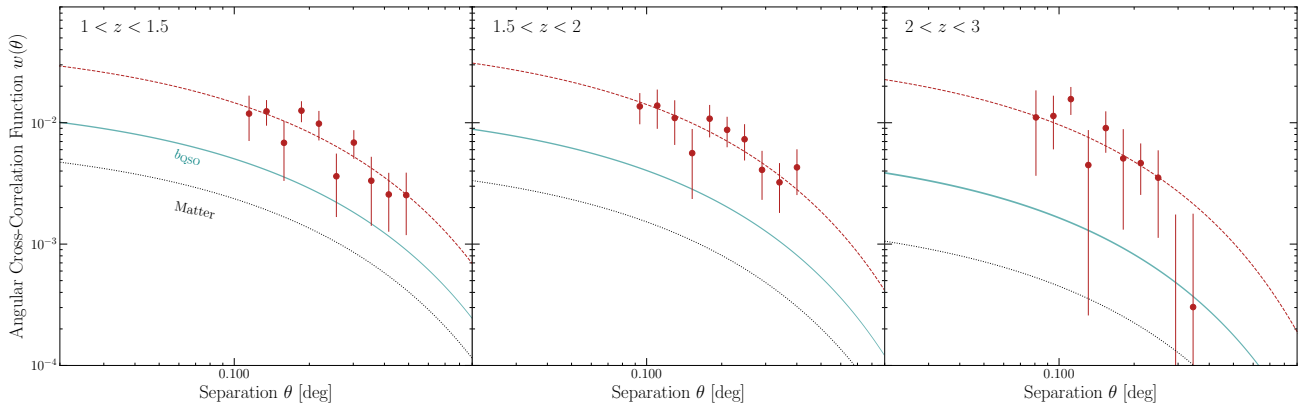

Figure 3. The tomographic angular cross correlation function measurements between HzRGs and eBOSS quasars in three redshift slices, displayed in the upper left corners. The linear matter model for the samples' redshift overlap is shown with a black dotted line, while the 1σ confidence interval of the quasar tracer bias is shown with teal bands. HzRGs are best fit with higher bias parameters than quasars, indicating they occupy more massive halos from $1 < z < 3$.

where J_0 is the zeroth-order Bessel function of the first kind, and $dN/dz_{i,j}$ are the normalized redshift distributions of the two tracers, identical in the case of an autocorrelation. For a linearly-biased model, the power spectrum is then given by bias factors multiplied by the matter power spectrum:

$$P_{ij}(k,z) = b_i b_j P_{\rm mm}(k,z). \tag{9}$$

We also model the spatial autocorrelations of eBOSS quasars and BOSS galaxies to interpret the tomographic cross-correlation measurements. This involves deducing the tracer bias by modeling the projected correlation functions (§4.3). The spatial correlation function $\xi(r)$ is the Fourier transform of the galaxy/quasar auto spectrum P_{gg}. The projected correlation function is then an Abel transform of $\xi(r)$:

$$w_p(r_p) = 2\int_{r_p}^{\infty} dr\, \frac{r\xi(r)}{\sqrt{r^2 - r_p^2}}. \tag{10}$$

5.1. *Modeling CMB Lensing*

We also model the cross-spectrum between radio galaxy overdensity and CMB lensing convergence. This is again given by a Limber (1953) integral over the lensing and galaxy projection kernels:

$$C_\ell^{\kappa g} = \int dz \frac{d\chi}{dz} \frac{W^\kappa W^g}{\chi^2} P_{\rm mm}\left(k = \frac{\ell + 1/2}{\chi},\, z\right) \tag{11}$$

where the CMB lensing kernel is given by (e.g., Cooray & Hu 2000):

$$W^\kappa(z) = \frac{3}{2}\Omega_{m,0}\left(\frac{H_0}{c}\right)^2 (1+z)\chi \frac{\chi_{\rm CMB} - \chi}{\chi_{\rm CMB}}, \tag{12}$$

and the linearly-biased galaxy overdensity kernel is:

$$W^g(z) = b\frac{dz}{d\chi}\frac{dN}{dz}. \tag{13}$$

The effective redshift at which we report the bias measurement is weighted by the lensing kernel (Modi et al. 2017; Krolewski et al. 2023):

$$z_{\rm eff} = \int dz \frac{d\chi}{dz}\frac{dN}{dz}\frac{z}{\chi^2} W^\kappa \tag{14}$$

We do not consider magnification bias, as we measure the response of number counts of our HzRG sample to limiting magnitude ($s_\mu \equiv d\ \log_{10} N/dm = 0.412 \pm 0.001$), which is sufficiently near the value of $s_\mu = 0.4$ for no magnification bias that any contribution is negligible.

5.2. *Halo Occupation Distribution Modeling*

We also model the radio galaxy autocorrelation functions in a halo occupation distribution (HOD) framework (Scoccimarro et al. 2001; Berlind & Weinberg 2002) for a more complete interpretation of how these systems occupy their host halos than the linear bias model. This entails replacing the power P_{ij} in Eq. 8 with an HOD power spectrum.

An HOD power spectrum is the sum of the "1-halo" power arising from pairs of galaxies in common halos, and the "2-halo" term from pairs between different halos. The HOD $\langle N(M)\rangle$ is the mean number of galaxies belonging to halos of mass M, decomposed into contributions from galaxies at the centers of halos, $\langle N_c(M)\rangle$, and secondary or 'satellite" galaxies belonging to the same halos $\langle N_s(M)\rangle$:

We adopt the HOD model of Zheng et al. (2007) and Zehavi et al. (2011), which implements the central occupation as a softened step function:

$$\langle N_c\rangle = \frac{1}{2}\left[1 + {\rm erf}\left(\frac{\log_{10}(M/M_{\rm min})}{\sigma_{\log_{10}M}}\right)\right] \tag{15}$$

where **erf** is the Gauss error function, $M_{\rm min}$ is the minimum halo mass required to host a radio galaxy, and $\sigma_{\log_{10}M}$ is the softening parameter. The satellite HOD is given then as:

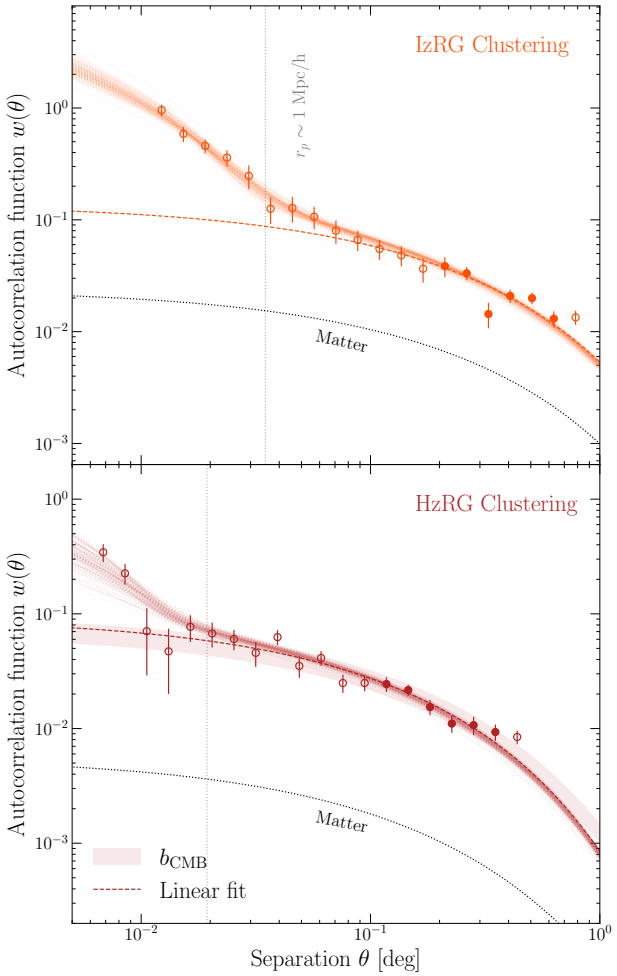

Figure 4. The autocorrelation function measurements of IzRGs (top panel in orange) and HzRGs (bottom panel in red). Filled markers show the measurements on linear projected scales ($5-25$ h^{-1} Mpc) at the median redshift of the sample, while open markers represent other scales. The projected scale of ~ 1 Mpc/h delineating the boundary of the one and two-halo terms is shown with vertical gray lines. The best fit of a linear model to the linear scales is shown with a dashed line. We also show the best fit HOD models to the full range of scales using transparent lines drawn from the posterior distributions.

$$\langle N_s \rangle = \Theta(M - M_0) \left(\frac{M - M_0}{M_1} \right)^{\alpha} \tag{16}$$

where Θ is the Heaviside step function, M_0 is the minimum mass to host a satellite quasar, and M_1 is the mass at which the term transitions to the power-law form. We enforce $M_0 = M_{\rm min}$ to reduce the model complexity, such that the minimum mass to host a central or satellite is identical. Our HOD models thus contain four free parameters, $M_{\rm min}$, $\sigma_{\log_{10} M}$, M_1, and α.

We compute the HOD power spectra given a set of parameters using the `Core Cosmology Library` (Chisari et al. 2019) package. Finally, unphysical one-halo power at large scales is suppressed using the Mead et al. (2021) prescription, and a smoothing is applied to intermediate scales between the one and two-halo regimes (Mead et al. 2015). We refer the reader to Petter et al. (2023) for additional details in the HOD modeling procedure. The observed autocorrelation functions are fit using the `emcee` (Foreman-Mackey et al. 2013) sampler, using broad priors of $\alpha = 1 \pm 0.3$, and $\ln(\sigma_{\log M}) = -0.5 \pm 0.5$ to avoid extremal values.

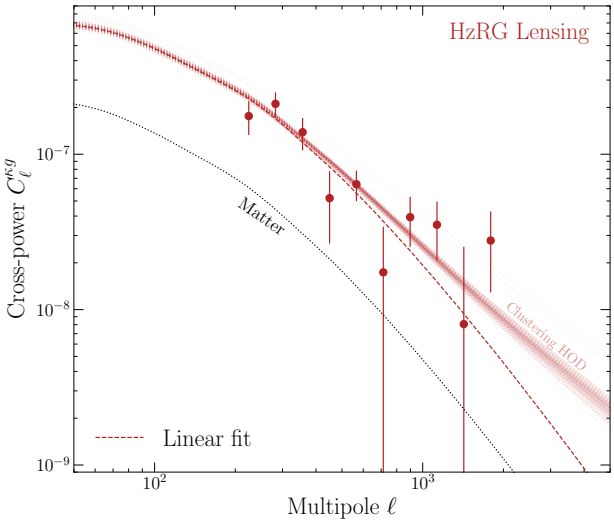

Figure 5. The cross correlation measurement of HzRG densities with *Planck* CMB lensing convergence κ. The matter spectrum for the redshift distribution is shown with a black dashed line, while the best linearly-biased fit is shown with a red dashed line. We also show the predictions of the lensing spectrum drawn from the HOD posterior fit to the autocorrelation clustering measurement (Fig. 4), demonstrating excellent agreement between the lensing and clustering analyses.

6. RESULTS

We can now interpret all of the observed autocorrelation functions, cross-correlations with CMB lensing, and cross-correlation functions with spectroscopic galaxy tracers in the halo model framework to constrain the environments in which radio galaxies release their energy.

6.1. *Effective halo masses*

We display the effective host halo mass results from all clustering measurements of luminous low-frequency radio galaxies at $z < 2.5$ in Fig. 6. These systems occupy massive halos of $\sim 10^{13} - 10^{13.5}$ $h^{-1} M_\odot$ for the past ~ 11 Gyr, with a possible mild increase in halo mass with cosmic time, consistent with the median growth rate of halos. We conclude that luminous radio galaxies are always hosted by group-scale halos, and that the occurrence of these systems is intimately connected to host halo mass (e.g.; Hatch et al. 2014). This a similar picture as for quasars, which occupy a lower but constant mass halo regime over time ($10^{12.5}$ $h^{-1} M_\odot$). These ob-

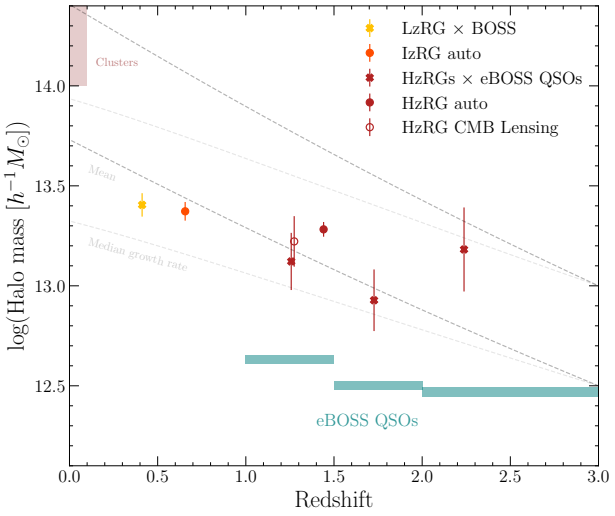

Figure 6. The effective halo masses of luminous low-frequency radio galaxies from $z < 2.5$. The red cross markers show the tomographic cross-correlations between eBOSS QSOs (halo masses shown with blue bands) and HzRGs. The solid circles in orange and red show the linear fits to the autocorrelations of IzRGs and HzRGs, and the open circle shows the result from HzRG CMB lensing. Radio galaxies are strongly clustered across cosmic time, in relatively constant halo masses. The median and mean halo growth rates from Fakhouri et al. (2010) are shown with dashed and dotted lines respectively, for halos whose progenitor masses were $10^{12.5}$ and $10^{13}h^{-1}M_\odot$ at z=3. The halos hosting luminous low-frequency radio galaxies at cosmic noon are expected to evolve on average into massive groups by the present.

servations support the paradigm where radiatively-inefficient accretion resulting in jets is driven by gas condensation from the hot halo, and may also reflect the fact that more massive halos contain more gas for jets to collide into and emit at low frequencies via shocks.

Though there are relatively few studies of radio galaxy environments at $z > 1$, our results at lower redshifts appear consistent with previous studies at $z < 1$. Clustering studies of radio galaxies at $z < 1$ reveal they exist in group environments (Mandelbaum et al. 2009; Hickox et al. 2009). This is consistent with studies of the galaxy overdensities surrounding $z < 1$ radio galaxies, showing they are on average found in galaxy groups (Best 2004; Ineson et al. 2015; Ching et al. 2017; Croston et al. 2019).

At higher redshift ($z > 1$), we find similar correspondence with previous results including clustering (Lindsay et al. 2014; Magliocchetti et al. 2017; Hale et al. 2018) and environmental (Hatch et al. 2014) studies, conducted at GHz frequencies. The lack of evolution in halo mass again supports the paradigm where radio galaxy activity must be intimately connected with the large-scale environment (Magliocchetti 2022).

6.2. *Halo occupation distributions*

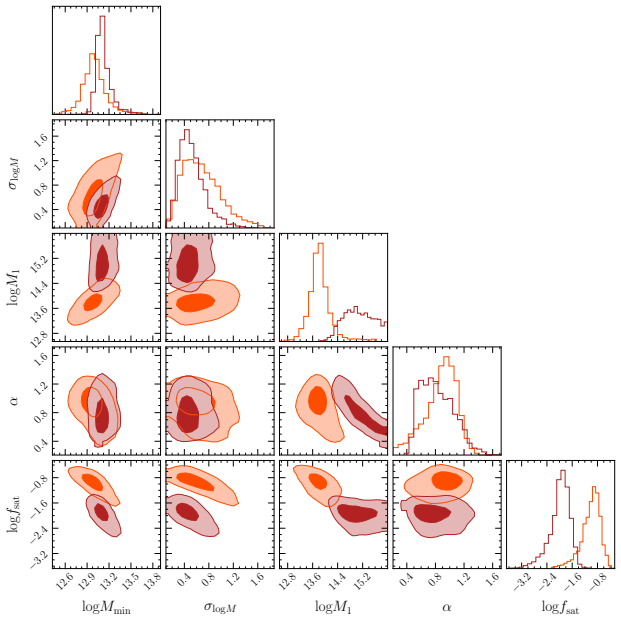

Figure 7. A corner plot of the HOD parameter posterior distributions (68 and 95% intervals) from fits to the autocorrelation functions of IzRGs (orange) and HzRGs (red). Though the samples occupy similar effective halo masses, their halo occupations may differ. Satellite radio galaxies appear to be hosted by lower-mass halos at $z \sim 0.7$ than at $z \sim 1.5$, such that the IzRG satellite fraction may be higher than for HzRGs.

For a more sophisticated interpretation of the manner in which radio galaxies occupy their host halos, we display the posterior distribution of HOD model fits to the autocorrelation functions of IzRGs and HzRGs in Figure 7. Though the samples at $z \sim 0.7$ and $z \sim 1.5$ are fit with similar effective halo masses, their full HODs reveal possible differences in the radio galaxy-halo connection over time. In particular, the stronger one-halo term of IzRGs (Figure 4) implies that satellite radio galaxies at $z \sim 0.7$ are hosted by lower mass halos than at $z \sim 1.5$. This in turn implies that luminous radio galaxies at lower redshift may be more often satellites in their halos than at higher redshift ($\sim 10\%$ vs $\sim 1\%$, respectively). We tentatively highlight that this may be connected to the evolution of star-forming properties, FRI/FRII status, and accretion mode from high to low redshift.

6.3. *Duty Cycle*

A constraint on the properties of halos hosting radio galaxies can be combined with the radio AGN luminosity function (LF) to constrain the occupation fraction or duty cycle of these systems. A comparison of the number density of radio galaxies in the sample to the number density of halos massive enough to host them yields the fraction of said halos at a given time which host an observable radio AGN. Assuming that every sufficiently massive halo hosts a central galaxy with a SMBH, this occupation fraction is interpreted

as a duty cycle $f_{\rm duty}$, or fraction of time that a SMBH hosted by these halos is observable as a radio galaxy in the survey (e.g., Haiman & Hui 2001; Martini & Weinberg 2001).

To estimate the radio galaxy duty cycle, we refit all clustering measurements (§4) with a minimum halo mass parameter $M_{\rm min}$ required to host a radio galaxy rather than the effective mass used before, using the relation between minimum mass and bias:

$$b(M > M_{\rm min}) = \frac{\int_{M_{\rm min}}^{\infty} dM \frac{dn}{dM} b(M)}{\int_{M_{\rm min}}^{\infty} dM \frac{dn}{dM}}. \quad (17)$$

We then estimate the space density of halos more massive than $M_{\rm min}$ by integrating the Tinker et al. (2008) halo mass function over mass and the considered redshift distribution. To estimate the space densities of the radio galaxies, we integrate the LoTSS-deep radio AGN LFs of Kondapally et al. (2022). We consider the best-fit LFs including all radio-excess AGNs, allowing for luminosity and density evolution, as presented in Kondapally et al. (2023). We account for the fact that our samples are limited by flux rather than luminosity by integrating above an evolving luminosity threshold with interpolation between LFs measured in different redshift epochs. At $z < 0.5$ where a best-fit LF is not provided, we interpolate between the LF measured at $0.5 < z < 1$, and the local ($z < 0.3$) LF from Sabater et al. (2019) and Kondapally et al. (2022). We adopt the local LF of Kondapally et al. (2022) at $L_{150\ \rm MHz} < 10^{26}$ W/Hz, and the LF of Sabater et al. (2019) above this limit, for reasons discussed in Kondapally et al. (2022), though choosing one or the other does not change the interpretation of our results.

We display the resulting duty cycle estimates in Figure 8. Luminous low-frequency radio galaxies exhibit duty cycles of $\sim 10\%$ since $z < 2.5$, roughly constant over the past 11 Gyr. The characteristic observable lifetime is thus $\sim$1 Gyr, consistent with the estimate of (Magliocchetti et al. 2017). Thus, rather than rising and falling before and after cosmic noon like quasar activity (Laurent et al. 2017), radio galaxy activity appears to be a more frequent and stable form of feedback. Radio galaxies are clearly more frequently switched on at $z < 1$, reaching rough parity with quasars at $z \sim 2$, and perhaps exceeding again at $z \gtrsim 2$. This highlights the importance of constraining radio galaxy clustering at $z \sim 3$.

6.4. *Heating Power per Halo*

Having constrained the host halo masses and duty cycles of luminous radio galaxies, we can now consider the energetics of the heating they supply to their environments. Here, we estimate the time-averaged kinetic heating power injected per host halo, and compare this to the same quantity for radiatively-driven quasar winds across cosmic time.

Kondapally et al. (2023) recently estimated the kinetic heating rate of LoTSS-deep radio galaxies as a function of 150 MHz luminosity - known as a specific heating rate $\Psi(L_{150}, z)$ - by convolving the luminosity functions of Kondapally et al. (2022) with a conversion between luminosity and kinetic jet power. They use the Heckman & Best (2014) relation calibrated using X-ray cluster cavities to trace the work done by jets observed at 1.4 GHz (Bîrzan et al. 2008; Cavagnolo et al. 2010). This heating rate thus specifies the kinetic power released into a unit volume as a function of radio luminosity. Kondapally et al. (2023) finds that the total heating is dominated by relatively high-luminosity sources ($L_{150} \gtrsim 10^{25}$ W/Hz), similar to our sample. They find that the total heating is dominated by LERGs, and that the global kinetic heating dominates over radiative quasar-mode feedback since $z \lesssim 2$. However, as quasars and radio galaxies occupy halos differently, a more meaningful comparison is the energy injected per host halo. In particular, we estimate the kinetic power injected into group-scale ($> 10^{13} h^{-1} M_{\odot}$) halos.

We integrate the Kondapally et al. (2023) specific heating rates (for all radio-excess AGNs) over luminosity using the flux limit of our sample at each redshift, yielding a total kinetic heating power sourced from these jets per unit volume, a kinetic luminosity density $\Omega_{\rm kin}(z)$. The time-averaged total heating power per halo is then the duty cycle multiplied by the luminosity density, divided by the number density of halos hosting these objects.

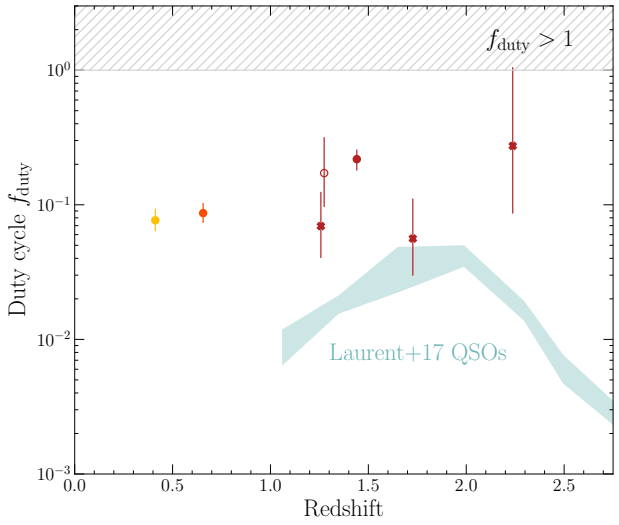

Figure 8. The duty cycle of luminous low-frequency radio galaxies over $z < 3$ implied by our clustering measurements and the luminosity functions of Kondapally et al. (2022). These systems appear to be active for $\sim 10\%$ of the Hubble time. We also show the 1σ confidence interval for the duty cycle of eBOSS quasars determined by Laurent et al. (2017) with a teal band. While quasar activity rises and falls before and after $z \sim 2$, radio galaxies maintain a constant duty cycle over 11 Gyr.

$$P_{\rm kin,halo} = f_{\rm duty} \frac{\int_{L_{\rm min}} dL \Psi(L,z)}{\int_{M_{\rm min}} dM_h \frac{dN_h}{dM_h}} \quad (18)$$

We can now compare this energy output to that of radiative-mode quasars kinetic contribution in the form of winds. Hopkins et al. (2007) estimated the cumulative bolometric energy released by quasars over time by integrating their quasar luminosity functions under the Soltan (1982) argument, assuming a 10% radiative efficiency. Only a fraction of this energy is ultimately transferred to kinetic energy in gaseous winds, found to vary considerably between studies ($0.0001\% - 1\%$; Fiore et al. 2017; Lutz et al. 2020; Dall'Agnol de Oliveira et al. 2021; Kakkad et al. 2022). Like Kondapally et al. (2023), here we adopt a characteristic range of $0.1 - 0.5\%$. To compute the average quasar-driven wind power density, we multiply this factor by the bolometric energy released per unit of cosmological time within a redshift interval. To estimate the average kinetic power per halo, we must next consider the density of massive halos hosting quasars.

The number density of massive halos hosting quasars depends on the quasar HOD. The masses of halos hosting Type-1 quasars appear remarkably consistent since $z \sim 6$ (Porciani et al. 2004; Croom et al. 2005; Porciani & Norberg 2006; Shen et al. 2007; Myers et al. 2007; da Ângela et al. 2008; Padmanabhan et al. 2009; Eftekharzadeh et al. 2015; Laurent et al. 2017; Geach et al. 2019; Timlin et al. 2018; He et al. 2018; Petter et al. 2022; Arita et al. 2023; Yuan et al. 2023; Prada et al. 2023), a few times $10^{12} h^{-1} M_\odot$. The full quasar HOD (Richardson et al. 2012; Eftekharzadeh et al. 2019) and its possible evolution or luminosity dependence has remained difficult to study. To estimate the radiative kinetic power released into group-scale halos ($> 10^{13} h^{-1} M_\odot$), we adopt the quasar HOD of Prada et al. (2023), assuming that it is valid across cosmic time. This implies that $\sim 5\%$ of quasars belong to group-scale halos (i.e., $\sim 5\%$ are satellites), and thus assuming that the HOD is luminosity independent, $\sim 5\%$ of the global quasar luminosity density is hosted by group-scale halos.

We display the time-averaged kinetic power injected by the radio galaxies studied in this work into their environments of group-scale halos ($M_h > 10^{13} h^{-1} M_\odot$) in Figure 9. We also show the contribution that quasar wind activity is expected to provide in these halos over time with a blue band. Due to the relatively constant clustering, luminosity function, and duty cycle of radio galaxies across time, these systems contribute an average 10^{42} erg/s of heating energy to their environments. Alternatively, the strong evolution of the quasar luminosity function along with the constant host halo mass implies that the contribution of quasar winds to heating group-halo gas falls with cosmic time. In particular, even assuming the maximum observed conversion efficiency between quasar luminosity and wind power, the radio galaxies studied in this work clearly dominate the heating budget at $z \lesssim 1$. This analysis shows that radio-mode feedback has been dominant over quasar-wind feedback in group halos for at least the past ~ 7 Gyr.

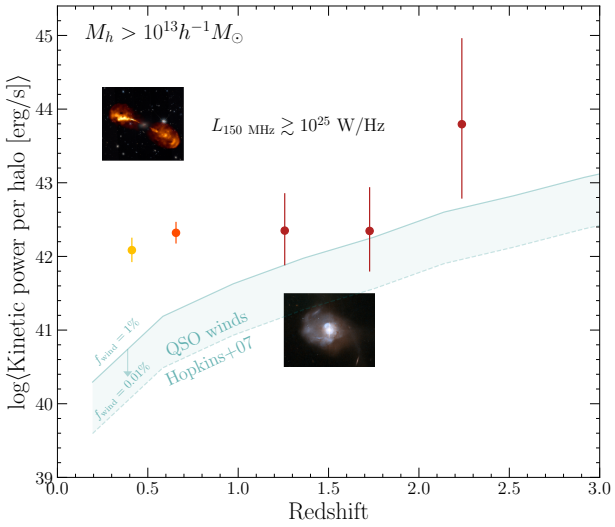

Figure 9. The time-averaged kinetic (heating) power injected into group-scale halos ($M_h > 10^{13} h^{-1} M_\odot$) by the radio galaxies studied in this work. Combining the clustering, duty cycle, and kinetic luminosity density of Kondapally et al. (2023) gives the expected power deposited per halo (Eq. 18). The teal band shows an estimated possible range of heating power deposited by radiative-mode quasars in the same halos, where the band ranges from wind fractions relative to bolometric luminosities of $0.01 - 1\%$. The average quasar wind heating power declines over cosmic time, due to the roughly constant host halo mass and steeply evolving luminosity function. Meanwhile, radio galaxies appear to contribute roughly constant mean power of $\sim 10^{42}$ erg/s over the past ~ 11 Gyr. Luminous radio galaxies thus dominate the heating input into massive halos over quasar winds since at least $z \sim 1$. We note that these results may be subject to substantial systematic uncertainties in the conversion between radio luminosity and mechanical power (Kondapally et al. 2023).

We raise the caveat that considering only Type-1 / unobscured quasars may provide an incomplete picture of radiatively-driven winds. Obscured quasars are canonically obscured by orientation with the line of sight, but a growing body of evidence may instead favor an evolutionary model of obscuration (Sanders et al. 1988; Alexander & Hickox 2012; Hickox & Alexander 2018), where some quasars are obscured by galactic or circumnuclear gas during an evolutionary phase. Obscured / reddened quasars are sometimes observed to be more strongly clustered than unobscured systems (Hickox et al. 2011; Donoso et al. 2014; DiPompeo et al. 2017; Petter et al. 2023), occupy galaxies forming stars more vigorously (Chen et al. 2015; Andonie et al. 2022), and show enhanced radio emission (Klindt et al. 2019), possibly tracing winds (Rosario et al. 2021). The strong clustering

and duty cycle of $\sim 10\%$ (Petter et al. 2023) are similar to the radio galaxies studied in this work, suggesting a possible stronger influence on the halos considered here compared to unobscured quasars. However, further constraints on obscured quasars' clustering evolution, their luminosity functions, and their radiation-wind coupling efficiency will be required to make meaningful constraints on their contribution to kinetic feedback.

We note that the conversion rate between observed radio luminosity and mechanical power is subject to significant systematic uncertainties (Willott et al. 1999; Hardcastle & Krause 2013; Hardcastle 2018). Therefore, further calibration of such a relation at 150 MHz and at high redshift, along with more precise clustering measurements are required to uncover which form of feedback dominates in massive halos at high redshift.

7. CONCLUSIONS

In this work, we select luminous ($L_{150\ \mathrm{MHz}} \gtrsim 10^{25}$ W/Hz) low-frequency radio galaxies on the basis of 150 MHz flux, bin them into redshift epochs using infrared counterparts, and study the evolution of their clustering properties from $z < 3$. We summarize our results as follows:

- These systems are strongly clustered across time, hosted by massive halos ($\sim 10^{13}-10^{13.5}h^{-1}M_{\odot}$). There is a tentative trend of a modest increase of effective halo mass with cosmic time, consistent with the median growth rate of the halos themselves. The high halo mass suggests that the triggering of low-frequency radio galaxy activity is strongly linked to the surrouding large-scale environment.

- The limited evolution both of the clustering and luminosity function implies that the duty cycle of these systems is a constant $\sim 10\%$ for the past 11 Gyr. The characteristic observable lifetime of these systems is $\sim$1 Gyr. These systems are active more frequently than quasars at $z < 1$, and perhaps also at $z > 2$.

- The constant clustering is interesting in the context of the evolution of source classification. This sample is dominated by star-forming galaxies with a mix of HERGs and LERGs at high redshift, and by quiescent LERGs since $z < 1$. The hosts of these systems at cosmic noon are expected to evolve on average into massive groups by the present.

- The kinetic power injected into group halos is dominated by radio galaxies rather than radiatively-efficient quasar wind power since at least $z \lesssim 1$. Radio galaxies are thus expected to be more efficient drivers of feedback in massive systems for at least the last 7 Gyr. At $z > 1$, uncertainties in the conversion from radio luminosity to kinetic power, the fraction of quasar luminosity coupled to winds, and the HODs of radio galaxies and quasars obscure the relative contribution of jets and winds.

The upcoming WEAVE-LOFAR spectroscopic follow up survey of LoTSS-detected sources (Smith et al. 2016) will improve precision on the clustering properties of radio galaxies, mitigate against any systematics in the radio galaxy redshift distribution, and possibly support separately studying clustering for LERGs and HERGs. Furthermore, upcoming sub-arcsecond imaging (Sweijen et al. 2022) of the LoTSS-wide area using the International LOFAR baselines should allow purer selection of radio galaxies to fainter fluxes using brightness temperature criteria (Morabito et al. 2022). Higher-resolution imaging should also allow for more precise cross-matching at alternate wavelengths, and enable clustering studies as a function of jet morphology. Finally, future X-ray missions such as *Athena* (Nandra et al. 2013) will detect the gas in groups and clusters out to $z \sim 2$ heated in part by the systems studied in this work.

This work shows that jet-mode feedback is the dominant source of heating in massive environments at $z < 1$. However, further constraints on the clustering of high-z radio galaxies, and the conversions between radio luminosity and mechanical power are required to perform a census of jet-mode feedback, and uncover the complete picture of how supermassive black hole accretion shapes galaxy growth across time.

ACKNOWLEDGMENTS

GCP acknowledges support from the Dartmouth Fellowship.

Facilities: LOFAR, SDSS, eBOSS, *WISE*, IRSA, *Planck*, *Spitzer*

Software: astropy: Astropy Collaboration et al. (2013), CAMB: Lewis et al. (2000), CCL: Chisari et al. (2019), colossus: Diemer (2018), Corrfunc: Sinha & Garrison (2020), emcee: Foreman-Mackey et al. (2013), HEALPix: Górski et al. (2005) , MANGLE: Hamilton & Tegmark (2004), TOPCAT: Taylor (2005).

REFERENCES

Alexander, D. M., & Hickox, R. C. 2012, NewAR, 56, 93, doi: 10.1016/j.newar.2011.11.003

Alexander, D. M., Swinbank, A. M., Smail, I., McDermid, R., & Nesvadba, N. P. H. 2010, MNRAS, 402, 2211, doi: 10.1111/j.1365-2966.2009.16046.x

Alonso, D., Bellini, E., Hale, C., Jarvis, M. J., & Schwarz, D. J. 2021, MNRAS, 502, 876, doi: 10.1093/mnras/stab046

Alonso, D., Sanchez, J., Slosar, A., & LSST Dark Energy Science Collaboration. 2019, MNRAS, 484, 4127, doi: 10.1093/mnras/stz093

Andonie, C., Alexander, D. M., Rosario, D., et al. 2022, MNRAS, 517, 2577, doi: 10.1093/mnras/stac2800

Arita, J., Kashikawa, N., Matsuoka, Y., et al. 2023, arXiv e-prints, arXiv:2307.02531, doi: 10.48550/arXiv.2307.02531

Assef, R. J., Stern, D., Noirot, G., et al. 2018, ApJS, 234, 23, doi: 10.3847/1538-4365/aaa00a

Astropy Collaboration, Robitaille, T. P., Tollerud, E. J., et al. 2013, A&A, 558, A33, doi: 10.1051/0004-6361/201322068

Balogh, M. L., Pearce, F. R., Bower, R. G., & Kay, S. T. 2001, MNRAS, 326, 1228, doi: 10.1111/j.1365-2966.2001.04667.x

Becker, R. H., White, R. L., & Helfand, D. J. 1995, ApJ, 450, 559, doi: 10.1086/176166

Benson, A. J., Bower, R. G., Frenk, C. S., et al. 2003, ApJ, 599, 38, doi: 10.1086/379160

Berlind, A. A., & Weinberg, D. H. 2002, ApJ, 575, 587, doi: 10.1086/341469

Best, P. N. 2004, MNRAS, 351, 70, doi: 10.1111/j.1365-2966.2004.07752.x

Best, P. N., Kaiser, C. R., Heckman, T. M., & Kauffmann, G. 2006, MNRAS, 368, L67, doi: 10.1111/j.1745-3933.2006.00159.x

Best, P. N., Kondapally, R., Williams, W. L., et al. 2023, MNRAS, 523, 1729, doi: 10.1093/mnras/stad1308

Binney, J., & Tabor, G. 1995, MNRAS, 276, 663, doi: 10.1093/mnras/276.2.663

Bîrzan, L., McNamara, B. R., Nulsen, P. E. J., Carilli, C. L., & Wise, M. W. 2008, ApJ, 686, 859, doi: 10.1086/591416

Bîrzan, L., Rafferty, D. A., McNamara, B. R., Wise, M. W., & Nulsen, P. E. J. 2004, ApJ, 607, 800, doi: 10.1086/383519

Boehringer, H., Voges, W., Fabian, A. C., Edge, A. C., & Neumann, D. M. 1993, MNRAS, 264, L25, doi: 10.1093/mnras/264.1.L25

Borgani, S., Murante, G., Springel, V., et al. 2004, MNRAS, 348, 1078, doi: 10.1111/j.1365-2966.2004.07431.x

Bower, R. G., Benson, A. J., Malbon, R., et al. 2006, MNRAS, 370, 645, doi: 10.1111/j.1365-2966.2006.10519.x

Brusa, M., Bongiorno, A., Cresci, G., et al. 2015, MNRAS, 446, 2394, doi: 10.1093/mnras/stu2117

Carilli, C. L., Perley, R. A., & Harris, D. E. 1994, MNRAS, 270, 173, doi: 10.1093/mnras/270.1.173

Carron, J., Mirmelstein, M., & Lewis, A. 2022, JCAP, 2022, 039, doi: 10.1088/1475-7516/2022/09/039

Cattaneo, A., Faber, S. M., Binney, J., et al. 2009, Nature, 460, 213, doi: 10.1038/nature08135

Cavagnolo, K. W., Donahue, M., Voit, G. M., & Sun, M. 2008, ApJL, 683, L107, doi: 10.1086/591665

Cavagnolo, K. W., McNamara, B. R., Nulsen, P. E. J., et al. 2010, ApJ, 720, 1066, doi: 10.1088/0004-637X/720/2/1066

Chen, C.-T. J., Hickox, R. C., Alberts, S., et al. 2015, ApJ, 802, 50, doi: 10.1088/0004-637X/802/1/50

Chiang, Y.-K., & Ménard, B. 2019, ApJ, 870, 120, doi: 10.3847/1538-4357/aaf4f6

Ching, J. H. Y., Croom, S. M., Sadler, E. M., et al. 2017, MNRAS, 469, 4584, doi: 10.1093/mnras/stx1173

Chisari, N. E., Alonso, D., Krause, E., et al. 2019, ApJS, 242, 2, doi: 10.3847/1538-4365/ab1658

Churazov, E., Forman, W., Jones, C., & Böhringer, H. 2000, A&A, 356, 788, doi: 10.48550/arXiv.astro-ph/0002375

Cooray, A., & Hu, W. 2000, ApJ, 534, 533, doi: 10.1086/308799

Cooray, A., & Sheth, R. 2002, PhR, 372, 1, doi: 10.1016/S0370-1573(02)00276-4

Croom, S. M., Boyle, B. J., Shanks, T., et al. 2005, MNRAS, 356, 415, doi: 10.1111/j.1365-2966.2004.08379.x

Croston, J. H., Hardcastle, M. J., Mingo, B., et al. 2019, A&A, 622, A10, doi: 10.1051/0004-6361/201834019

Croton, D. J., Springel, V., White, S. D. M., et al. 2006, MNRAS, 365, 11, doi: 10.1111/j.1365-2966.2005.09675.x

Croton, D. J., Stevens, A. R. H., Tonini, C., et al. 2016, ApJS, 222, 22, doi: 10.3847/0067-0049/222/2/22

da Ângela, J., Shanks, T., Croom, S. M., et al. 2008, MNRAS, 383, 565, doi: 10.1111/j.1365-2966.2007.12552.x

Dall'Agnol de Oliveira, B., Storchi-Bergmann, T., Kraemer, S. B., et al. 2021, MNRAS, 504, 3890, doi: 10.1093/mnras/stab1067

Davé, R., Anglés-Alcázar, D., Narayanan, D., et al. 2019, MNRAS, 486, 2827, doi: 10.1093/mnras/stz937

Davis, M., & Peebles, P. J. E. 1983, ApJ, 267, 465, doi: 10.1086/160884

Dawson, K. S., Schlegel, D. J., Ahn, C. P., et al. 2013, AJ, 145, 10, doi: 10.1088/0004-6256/145/1/10

Dawson, K. S., Kneib, J.-P., Percival, W. J., et al. 2016, AJ, 151, 44, doi: 10.3847/0004-6256/151/2/44

DESI Collaboration, Adame, A. G., Aguilar, J., et al. 2023, arXiv e-prints, arXiv:2306.06308, doi: 10.48550/arXiv.2306.06308

Dey, A., Schlegel, D. J., Lang, D., et al. 2019, AJ, 157, 168, doi: 10.3847/1538-3881/ab089d

Di Matteo, T., Springel, V., & Hernquist, L. 2005, Nature, 433, 604, doi: 10.1038/nature03335

Diemer, B. 2018, ApJS, 239, 35, doi: 10.3847/1538-4365/aaee8c

DiPompeo, M. A., Hickox, R. C., Eftekharzadeh, S., & Myers, A. D. 2017, MNRAS, 469, 4630, doi: 10.1093/mnras/stx1215
Donahue, M., & Voit, G. M. 2022, PhR, 973, 1, doi: 10.1016/j.physrep.2022.04.005
Donoso, E., Yan, L., Stern, D., & Assef, R. J. 2014, ApJ, 789, 44, doi: 10.1088/0004-637X/789/1/44
Duffy, A. R., Schaye, J., Kay, S. T., & Dalla Vecchia, C. 2008, MNRAS, 390, L64, doi: 10.1111/j.1745-3933.2008.00537.x
Duncan, K. J., Kondapally, R., Brown, M. J. I., et al. 2021, A&A, 648, A4, doi: 10.1051/0004-6361/202038809
Dunn, R. J. H., & Fabian, A. C. 2008, MNRAS, 385, 757, doi: 10.1111/j.1365-2966.2008.12898.x
Edge, A. C., Stewart, G. C., & Fabian, A. C. 1992, MNRAS, 258, 177, doi: 10.1093/mnras/258.1.177
Eftekharzadeh, S., Myers, A. D., & Kourkchi, E. 2019, MNRAS, 486, 274, doi: 10.1093/mnras/stz770
Eftekharzadeh, S., Myers, A. D., White, M., et al. 2015, MNRAS, 453, 2779, doi: 10.1093/mnras/stv1763
Elvis, M. 2000, ApJ, 545, 63, doi: 10.1086/317778
Fabian, A. C. 2012, ARA&A, 50, 455, doi: 10.1146/annurev-astro-081811-125521
Fabian, A. C., Sanders, J. S., Taylor, G. B., et al. 2006, MNRAS, 366, 417, doi: 10.1111/j.1365-2966.2005.09896.x
Fakhouri, O., Ma, C.-P., & Boylan-Kolchin, M. 2010, MNRAS, 406, 2267, doi: 10.1111/j.1365-2966.2010.16859.x
Fiore, F., Feruglio, C., Shankar, F., et al. 2017, A&A, 601, A143, doi: 10.1051/0004-6361/201629478
Foreman-Mackey, D., Hogg, D. W., Lang, D., & Goodman, J. 2013, PASP, 125, 306, doi: 10.1086/670067
Geach, J. E., Peacock, J. A., Myers, A. D., et al. 2019, ApJ, 874, 85, doi: 10.3847/1538-4357/ab0894
Gonzalez-Perez, V., Lacey, C. G., Baugh, C. M., et al. 2014, MNRAS, 439, 264, doi: 10.1093/mnras/stt2410
Górski, K. M., Hivon, E., Banday, A. J., et al. 2005, ApJ, 622, 759, doi: 10.1086/427976
Greene, J. E., Pooley, D., Zakamska, N. L., Comerford, J. M., & Sun, A.-L. 2014, ApJ, 788, 54, doi: 10.1088/0004-637X/788/1/54
Gürkan, G., Hardcastle, M. J., Best, P. N., et al. 2019, A&A, 622, A11, doi: 10.1051/0004-6361/201833892
Haiman, Z., & Hui, L. 2001, ApJ, 547, 27, doi: 10.1086/318330
Hale, C. L., Jarvis, M. J., Delvecchio, I., et al. 2018, MNRAS, 474, 4133, doi: 10.1093/mnras/stx2954
Hamilton, A. J. S., & Tegmark, M. 2004, MNRAS, 349, 115, doi: 10.1111/j.1365-2966.2004.07490.x
Hardcastle, M. J. 2018, MNRAS, 475, 2768, doi: 10.1093/mnras/stx3358
Hardcastle, M. J., & Croston, J. H. 2020, NewAR, 88, 101539, doi: 10.1016/j.newar.2020.101539
Hardcastle, M. J., & Krause, M. G. H. 2013, MNRAS, 430, 174, doi: 10.1093/mnras/sts564
Hardcastle, M. J., Williams, W. L., Best, P. N., et al. 2019, A&A, 622, A12, doi: 10.1051/0004-6361/201833893
Hardcastle, M. J., Horton, M. A., Williams, W. L., et al. 2023, arXiv e-prints, arXiv:2309.00102, doi: 10.48550/arXiv.2309.00102
Harrison, C. M., Alexander, D. M., Mullaney, J. R., & Swinbank, A. M. 2014, MNRAS, 441, 3306, doi: 10.1093/mnras/stu515
Harrison, C. M., Alexander, D. M., Swinbank, A. M., et al. 2012, MNRAS, 426, 1073, doi: 10.1111/j.1365-2966.2012.21723.x
Hatch, N. A., Wylezalek, D., Kurk, J. D., et al. 2014, MNRAS, 445, 280, doi: 10.1093/mnras/stu1725
He, W., Akiyama, M., Bosch, J., et al. 2018, PASJ, 70, S33, doi: 10.1093/pasj/psx129
Heckman, T. M., & Best, P. N. 2014, ARA&A, 52, 589, doi: 10.1146/annurev-astro-081913-035722
Helfand, D. J., White, R. L., & Becker, R. H. 2015, ApJ, 801, 26, doi: 10.1088/0004-637X/801/1/26
Hickox, R. C., & Alexander, D. M. 2018, ARA&A, 56, 625, doi: 10.1146/annurev-astro-081817-051803
Hickox, R. C., Jones, C., Forman, W. R., et al. 2009, ApJ, 696, 891, doi: 10.1088/0004-637X/696/1/891
Hickox, R. C., Myers, A. D., Brodwin, M., et al. 2011, ApJ, 731, 117, doi: 10.1088/0004-637X/731/2/117
Hivon, E., Górski, K. M., Netterfield, C. B., et al. 2002, ApJ, 567, 2, doi: 10.1086/338126
Hopkins, P. F., Hernquist, L., Cox, T. J., et al. 2006, ApJS, 163, 1, doi: 10.1086/499298
Hopkins, P. F., Richards, G. T., & Hernquist, L. 2007, ApJ, 654, 731, doi: 10.1086/509629
Ineson, J., Croston, J. H., Hardcastle, M. J., et al. 2015, MNRAS, 453, 2682, doi: 10.1093/mnras/stv1807
Kaiser, N. 1987, MNRAS, 227, 1, doi: 10.1093/mnras/227.1.1
Kakkad, D., Sani, E., Rojas, A. F., et al. 2022, MNRAS, 511, 2105, doi: 10.1093/mnras/stac103
Kaviraj, S., Laigle, C., Kimm, T., et al. 2017, MNRAS, 467, 4739, doi: 10.1093/mnras/stx126
Klindt, L., Alexander, D. M., Rosario, D. J., Lusso, E., & Fotopoulou, S. 2019, MNRAS, 488, 3109, doi: 10.1093/mnras/stz1771
Kochanek, C. S., Eisenstein, D. J., Cool, R. J., et al. 2012, ApJS, 200, 8, doi: 10.1088/0067-0049/200/1/8
Kondapally, R., Best, P. N., Hardcastle, M. J., et al. 2021, A&A, 648, A3, doi: 10.1051/0004-6361/202038813
Kondapally, R., Best, P. N., Cochrane, R. K., et al. 2022, MNRAS, 513, 3742, doi: 10.1093/mnras/stac1128
Kondapally, R., Best, P. N., Raouf, M., et al. 2023, MNRAS, 523, 5292, doi: 10.1093/mnras/stad1813

Kormendy, J., & Ho, L. C. 2013, ARA&A, 51, 511, doi: 10.1146/annurev-astro-082708-101811
Krolewski, A., Ferraro, S., Schlafly, E. F., & White, M. 2020, JCAP, 2020, 047, doi: 10.1088/1475-7516/2020/05/047
Krolewski, A., Percival, W. J., Ferraro, S., et al. 2023, arXiv e-prints, arXiv:2305.07650, doi: 10.48550/arXiv.2305.07650
Laha, S., Reynolds, C. S., Reeves, J., et al. 2021, Nature Astronomy, 5, 13, doi: 10.1038/s41550-020-01255-2
Landy, S. D., & Szalay, A. S. 1993, ApJ, 412, 64, doi: 10.1086/172900
Laurent, P., Eftekharzadeh, S., Le Goff, J.-M., et al. 2017, JCAP, 2017, 017, doi: 10.1088/1475-7516/2017/07/017
Lewis, A., Challinor, A., & Lasenby, A. 2000, ApJ, 538, 473, doi: 10.1086/309179
Limber, D. N. 1953, ApJ, 117, 134, doi: 10.1086/145672
Lindsay, S. N., Jarvis, M. J., & McAlpine, K. 2014, MNRAS, 440, 2322, doi: 10.1093/mnras/stu453
Lutz, D., Sturm, E., Janssen, A., et al. 2020, A&A, 633, A134, doi: 10.1051/0004-6361/201936803
Madau, P., & Dickinson, M. 2014, ARA&A, 52, 415, doi: 10.1146/annurev-astro-081811-125615
Madhavacheril, M. S., Qu, F. J., Sherwin, B. D., et al. 2023, arXiv e-prints, arXiv:2304.05203, doi: 10.48550/arXiv.2304.05203
Magliocchetti, M. 2022, A&A Rv, 30, 6, doi: 10.1007/s00159-022-00142-1
Magliocchetti, M., Popesso, P., Brusa, M., et al. 2017, MNRAS, 464, 3271, doi: 10.1093/mnras/stw2541
Magliocchetti, M., Maddox, S. J., Hawkins, E., et al. 2004, MNRAS, 350, 1485, doi: 10.1111/j.1365-2966.2004.07751.x
Magorrian, J., Tremaine, S., Richstone, D., et al. 1998, AJ, 115, 2285, doi: 10.1086/300353
Mandelbaum, R., Li, C., Kauffmann, G., & White, S. D. M. 2009, MNRAS, 393, 377, doi: 10.1111/j.1365-2966.2008.14235.x
Marocco, F., Eisenhardt, P. R. M., Fowler, J. W., et al. 2021a, ApJS, 253, 8, doi: 10.3847/1538-4365/abd805
—. 2021b, ApJS, 253, 8, doi: 10.3847/1538-4365/abd805
Marocco et al. 2020, CatWISE2020 Catalog, IPAC, doi: 10.26131/IRSA551
Martini, P., & Weinberg, D. H. 2001, ApJ, 547, 12, doi: 10.1086/318331
McCarthy, I. G., Schaye, J., Ponman, T. J., et al. 2010, MNRAS, 406, 822, doi: 10.1111/j.1365-2966.2010.16750.x
McNamara, B. R., & Nulsen, P. E. J. 2007, ARA&A, 45, 117, doi: 10.1146/annurev.astro.45.051806.110625
—. 2012, New Journal of Physics, 14, 055023, doi: 10.1088/1367-2630/14/5/055023
McNamara, B. R., Wise, M., Nulsen, P. E. J., et al. 2000, ApJL, 534, L135, doi: 10.1086/312662
Mead, A. J., Brieden, S., Tröster, T., & Heymans, C. 2021, MNRAS, 502, 1401, doi: 10.1093/mnras/stab082
Mead, A. J., Peacock, J. A., Heymans, C., Joudaki, S., & Heavens, A. F. 2015, MNRAS, 454, 1958, doi: 10.1093/mnras/stv2036
Ménard, B., Scranton, R., Schmidt, S., et al. 2013, arXiv e-prints, arXiv:1303.4722, doi: 10.48550/arXiv.1303.4722
Modi, C., White, M., & Vlah, Z. 2017, JCAP, 2017, 009, doi: 10.1088/1475-7516/2017/08/009
Morabito, L. K., Sweijen, F., Radcliffe, J. F., et al. 2022, MNRAS, 515, 5758, doi: 10.1093/mnras/stac2129
Myers, A. D., Brunner, R. J., Nichol, R. C., et al. 2007, ApJ, 658, 85, doi: 10.1086/511519
Myers, A. D., Palanque-Delabrouille, N., Prakash, A., et al. 2015, ApJS, 221, 27, doi: 10.1088/0067-0049/221/2/27
Nandra, K., Barret, D., Barcons, X., et al. 2013, arXiv e-prints, arXiv:1306.2307, doi: 10.48550/arXiv.1306.2307
Narayan, R., & Yi, I. 1994, ApJL, 428, L13, doi: 10.1086/187381
Navarro, J. F., Frenk, C. S., & White, S. D. M. 1997, ApJ, 490, 493, doi: 10.1086/304888
Newman, J. A. 2008, ApJ, 684, 88, doi: 10.1086/589982
Omori, Y., Baxter, E. J., Chang, C., et al. 2023, PhRvD, 107, 023529, doi: 10.1103/PhysRevD.107.023529
Padmanabhan, N., White, M., Norberg, P., & Porciani, C. 2009, MNRAS, 397, 1862, doi: 10.1111/j.1365-2966.2008.14071.x
Peacock, J. A. 1991, MNRAS, 253, 1P, doi: 10.1093/mnras/253.1.1P
Peebles, P. J. E. 1980, The large-scale structure of the universe
Petter, G. C., Hickox, R. C., Alexander, D. M., et al. 2023, ApJ, 946, 27, doi: 10.3847/1538-4357/acb7ef
—. 2022, ApJ, 927, 16, doi: 10.3847/1538-4357/ac4d31
Planck Collaboration, Aghanim, N., Akrami, Y., et al. 2020, A&A, 641, A6, doi: 10.1051/0004-6361/201833910
Porciani, C., Magliocchetti, M., & Norberg, P. 2004, MNRAS, 355, 1010, doi: 10.1111/j.1365-2966.2004.08408.x
Porciani, C., & Norberg, P. 2006, MNRAS, 371, 1824, doi: 10.1111/j.1365-2966.2006.10813.x
Prada, F., Ereza, J., Smith, A., et al. 2023, arXiv e-prints, arXiv:2306.06315, doi: 10.48550/arXiv.2306.06315
Reid, B., Ho, S., Padmanabhan, N., et al. 2016, MNRAS, 455, 1553, doi: 10.1093/mnras/stv2382
Rennehan, D., Babul, A., Moa, B., & Davé, R. 2023, arXiv e-prints, arXiv:2309.15898. https://arxiv.org/abs/2309.15898
Rezaie, M., Ross, A. J., Seo, H.-J., et al. 2021, MNRAS, 506, 3439, doi: 10.1093/mnras/stab1730
Richardson, J., Zheng, Z., Chatterjee, S., Nagai, D., & Shen, Y. 2012, ApJ, 755, 30, doi: 10.1088/0004-637X/755/1/30
Rosario, D. J., Alexander, D. M., Moldon, J., et al. 2021, MNRAS, 505, 5283, doi: 10.1093/mnras/stab1653
Ross, A. J., Bautista, J., Tojeiro, R., et al. 2020, MNRAS, 498, 2354, doi: 10.1093/mnras/staa2416
Rupke, D. S. N., & Veilleux, S. 2011, ApJL, 729, L27, doi: 10.1088/2041-8205/729/2/L27

Sabater, J., Best, P. N., Hardcastle, M. J., et al. 2019, A&A, 622, A17, doi: 10.1051/0004-6361/201833883
Sabater, J., Best, P. N., Tasse, C., et al. 2021, A&A, 648, A2, doi: 10.1051/0004-6361/202038828
Sanders, D. B., Soifer, B. T., Elias, J. H., Neugebauer, G., & Matthews, K. 1988, ApJL, 328, L35, doi: 10.1086/185155
Schaye, J., Crain, R. A., Bower, R. G., et al. 2015, MNRAS, 446, 521, doi: 10.1093/mnras/stu2058
Schlafly, E. F., Meisner, A. M., & Green, G. M. 2019, ApJS, 240, 30, doi: 10.3847/1538-4365/aafbea
Scoccimarro, R., Sheth, R. K., Hui, L., & Jain, B. 2001, ApJ, 546, 20, doi: 10.1086/318261
Seljak, U. 2000, MNRAS, 318, 203, doi: 10.1046/j.1365-8711.2000.03715.x
Shakura, N. I., & Sunyaev, R. A. 1973, A&A, 24, 337
Shen, Y., Strauss, M. A., Oguri, M., et al. 2007, AJ, 133, 2222, doi: 10.1086/513517
Shimwell, T. W., Röttgering, H. J. A., Best, P. N., et al. 2017, A&A, 598, A104, doi: 10.1051/0004-6361/201629313
Shimwell, T. W., Hardcastle, M. J., Tasse, C., et al. 2022, A&A, 659, A1, doi: 10.1051/0004-6361/202142484
Siewert, T. M., Hale, C., Bhardwaj, N., et al. 2020, A&A, 643, A100, doi: 10.1051/0004-6361/201936592
Silk, J., & Rees, M. J. 1998, A&A, 331, L1, doi: 10.48550/arXiv.astro-ph/9801013
Sinha, M., & Garrison, L. H. 2020, MNRAS, 491, 3022, doi: 10.1093/mnras/stz3157
Smith, D. J. B., Best, P. N., Duncan, K. J., et al. 2016, in SF2A-2016: Proceedings of the Annual meeting of the French Society of Astronomy and Astrophysics, ed. C. Reylé, J. Richard, L. Cambrésy, M. Deleuil, E. Pécontal, L. Tresse, & I. Vauglin, 271–280
Smolčić, V., Novak, M., Bondi, M., et al. 2017, A&A, 602, A1, doi: 10.1051/0004-6361/201628704
Soltan, A. 1982, MNRAS, 200, 115, doi: 10.1093/mnras/200.1.115
Somerville, R. S., & Davé, R. 2015, ARA&A, 53, 51, doi: 10.1146/annurev-astro-082812-140951
Somerville, R. S., Hopkins, P. F., Cox, T. J., Robertson, B. E., & Hernquist, L. 2008, MNRAS, 391, 481, doi: 10.1111/j.1365-2966.2008.13805.x
Springel, V., Di Matteo, T., & Hernquist, L. 2005, MNRAS, 361, 776, doi: 10.1111/j.1365-2966.2005.09238.x
Springel, V., Pakmor, R., Pillepich, A., et al. 2018, MNRAS, 475, 676, doi: 10.1093/mnras/stx3304
Sweijen, F., van Weeren, R. J., Röttgering, H. J. A., et al. 2022, Nature Astronomy, 6, 350, doi: 10.1038/s41550-021-01573-z
Tabor, G., & Binney, J. 1993, MNRAS, 263, 323, doi: 10.1093/mnras/263.2.323
Tasse, C., Shimwell, T., Hardcastle, M. J., et al. 2021, A&A, 648, A1, doi: 10.1051/0004-6361/202038804
Taylor, M. B. 2005, in Astronomical Society of the Pacific Conference Series, Vol. 347, Astronomical Data Analysis Software and Systems XIV, ed. P. Shopbell, M. Britton, & R. Ebert, 29
Thacker, R. J., Scannapieco, E., & Couchman, H. M. P. 2006, ApJ, 653, 86, doi: 10.1086/508650
Timlin, J. D., Ross, N. P., Richards, G. T., et al. 2018, ApJ, 859, 20, doi: 10.3847/1538-4357/aab9ac
Tinker, J., Kravtsov, A. V., Klypin, A., et al. 2008, ApJ, 688, 709, doi: 10.1086/591439
Tinker, J. L., Robertson, B. E., Kravtsov, A. V., et al. 2010, ApJ, 724, 878, doi: 10.1088/0004-637X/724/2/878
Tiwari, P., Zhao, R., Zheng, J., et al. 2022, ApJ, 928, 38, doi: 10.3847/1538-4357/ac5748
van Haarlem, M. P., Wise, M. W., Gunst, A. W., et al. 2013, A&A, 556, A2, doi: 10.1051/0004-6361/201220873
Veilleux, S., Cecil, G., & Bland-Hawthorn, J. 2005, ARA&A, 43, 769, doi: 10.1146/annurev.astro.43.072103.150610
Vogelsberger, M., Genel, S., Springel, V., et al. 2014, MNRAS, 444, 1518, doi: 10.1093/mnras/stu1536
White, S. D. M., & Frenk, C. S. 1991, ApJ, 379, 52, doi: 10.1086/170483
White, S. D. M., & Rees, M. J. 1978, MNRAS, 183, 341, doi: 10.1093/mnras/183.3.341
Willott, C. J., Rawlings, S., Blundell, K. M., & Lacy, M. 1999, MNRAS, 309, 1017, doi: 10.1046/j.1365-8711.1999.02907.x
Wright, E. L., Eisenhardt, P. R. M., Mainzer, A. K., et al. 2010, AJ, 140, 1868, doi: 10.1088/0004-6256/140/6/1868
York, D. G., Adelman, J., Anderson, John E., J., et al. 2000, AJ, 120, 1579, doi: 10.1086/301513
Yuan, S., Zhang, H., Ross, A. J., et al. 2023, arXiv e-prints, arXiv:2306.06314, doi: 10.48550/arXiv.2306.06314
Zakamska, N. L., Hamann, F., Pâris, I., et al. 2016, MNRAS, 459, 3144, doi: 10.1093/mnras/stw718
Zehavi, I., Zheng, Z., Weinberg, D. H., et al. 2011, ApJ, 736, 59, doi: 10.1088/0004-637X/736/1/59
Zheng, Z., Coil, A. L., & Zehavi, I. 2007, ApJ, 667, 760, doi: 10.1086/521074